### Title

Multiscale Characterization of the Influence of the Organic–Inorganic Interface on the Dielectric Breakdown of Nanocomposites




### Journal

ACS Nano, 16(4)

### ISSN

1936-0851



### Authors

Pieters, Priscilla F
Lainé, Antoine
Li, He
et al.



### Publication Date

2022-04-26

### DOI

10.1021/acsnano.2c01558

Peer reviewed

# Multiscale Characterization of the Influence of the Organic-Inorganic Interface on Dielectric Breakdown of Nanocomposites

*Priscilla F. Pieters,[a] Antoine Lainé,[b] He Li,[b,c] Yi-Hsien Lu,[b] Yashpal Singh,[b] Lin-Wang Wang,[b] Yi Liu,[b,c] Ting Xu,[a,b,d] A. Paul Alivisatos,[a,b,d,e,†] Miquel B. Salmeron[b,d,*]*

[a]Department of Chemistry, University of California, Berkeley, California 94720, United States

[b]Materials Sciences Division, Lawrence Berkeley National Laboratory, Berkeley, California 94720, United States

[c]Molecular Foundry, Lawrence Berkeley National Laboratory, Berkeley, California 94720, United States

[d]Department of Materials Science and Engineering, University of California, Berkeley, California 94720, United States

[e]Kavli Energy NanoScience Institute, Berkeley, California 94720, United States

[†]Present address: Department of Chemistry and Pritzker School of Molecular Engineering, University of Chicago, Chicago, Illinois 60637, United States

* To whom correspondence may be addressed: mbsalmeron@lbl.gov

Full article available at: https://doi.org/10.1021/acsnano.2c01558

ABSTRACT

Nanoscale engineered materials such as nanocomposites can display or be designed to enhance their material properties through control of the internal interfaces. Here, we unveil the nanoscale origin and important characteristics of the enhanced dielectric breakdown capabilities of gold nanoparticle/polymer nanocomposites. Our multiscale approach spans from the study of a single chemically designed organic/inorganic interface to micrometer-thick films. At the nanoscale, we relate the improved breakdown strength to the interfacial charge retention capability by combining scanning probe measurements and density functional theory calculations. At the meso- and macro-scale, our findings highlight the relevance of the nanoparticle concentration and distribution in determining and enhancing the dielectric properties, as well as identifying this as a crucial limiting factor for the achievable sample size.

KEYWORDS: interfaces, nanocomposites, self-assembled monolayers, dielectric breakdown, nanoparticles, charge retention, Kelvin probe force microscopy

Increasing energy demand and the need for improved energy storage solutions call for the development of high-performance dielectric materials with high power and energy densities, high breakdown strength, and facile processability. Dielectric capacitors are ideal for electrical power systems operating at high voltage, and advanced electronic devices. Compared to other energy storage techniques, they exhibit a high power density due to their fast charging and discharging.[1,2] The energy density $U$ inside capacitors is described by the following equation: $U = \frac{1}{2}\varepsilon_0\varepsilon_r E^2$, where $\varepsilon_0$ is the permittivity of free space, $\varepsilon_r$ is the relative dielectric permittivity, and $E$ is the applied electric field. The maximum energy density in the capacitor thus depends on the $\varepsilon_r$ of the material and is eventually limited by the film's dielectric breakdown strength ($E_{br}$). Ceramic dielectrics are commonly used dielectric materials due to their high $\varepsilon_r$, but offer a relatively low $E_{br}$, and poor processibility.[3] Polymers, on the other hand, have a relatively low $\varepsilon_r$, but are flexible and easily processible materials often exhibiting a high $E_{br}$.[4,5] Polymer nanocomposites aim to combine both of these advantageous properties to create materials with enhanced performance.

Interfacial engineering of these materials usually further accentuates such improvements as in nanocomposites, the properties of the material cannot simply be viewed as the sum of the properties of its components.[6] This key role of the interface in determining the final properties of the nanomaterial is evidenced by the increased operational stability against dielectric breakdown in nanocomposites.[7–10] Understanding the exact relation between the nanoscale interfaces on the overall macroscopic properties of the material still remains a formidable challenge. Together with precisely controlling the interfacial properties, the development of new high-performance dielectric materials will be facilitated.

Including nanoparticles (NPs) in a polymer matrix creates a large interfacial area that is highly polarizable and can concentrate a large number of charge carriers per volume.[10] Ceramic NPs, such as $BaTiO_3$, embedded in a polymer matrix, can substantially enhance the $\varepsilon_r$ of the composite. However, because of the mismatch between the $\varepsilon_r$ of the NP and the polymer matrix, the electric field distributes inhomogeneously around the interface and the electric field concentrates locally in the polymer matrix, which dramatically lowers the breakdown strength.[7,11] Efforts to circumvent this problem have mainly focused on interfacial engineering by surface modifications and by using core-shell materials.[12–14] Encasing $BaTiO_3$ nanofibers in a $TiO_2$ shell to act as an inorganic buffer layer effectively alleviates the local electric field distortion in the polymer matrix, as well as creates polarization and charge shifting limited to the inorganic interfacial zone.[8] A similar interfacial polarization in nanocomposites was recently imaged in poly(vinylidene fluoride-*co*-trifluoroethylene) (P(VDF-TrFE)) nanocomposites filled with $BaTiO_3$ NPs.[15,16] Kelvin-Probe Force Microscopy (KPFM) showed that space charges are trapped in the interfacial region around the embedded NPs when a DC electric field was applied. In addition, an enhanced chain mobility of the polymer is reported at the interfacial region, which results in a higher electric polarization at the interface.

Increasing the dielectric performance of nanocomposites can also be achieved by using conductive particles dispersed in a polymer matrix.[17–19] Such particles are expected to be fully polarized under an applied field, thus screening the electric field and displaying a theoretically infinite $\varepsilon_r$. Indeed, colossal $\varepsilon_r$ values have been observed for nanocomposites containing conductive fillers.[20,21] The conductive NPs serve as embedded electrodes surrounded by the polymer dielectric, resulting in an array of connected “nanocapacitors” inside the nanocomposite, leading to the large enhancement in $\varepsilon_r$.[22] The polarization of the dielectric

between the NPs further increases the apparent $\varepsilon_r$, similar to grain-boundary barrier layer ceramic capacitors. However, increasing the filler loading up to the percolation threshold results in the formation of a conductive pathway along the NPs chain and consequently a dramatic loss of dielectric capabilities.[23,24] Additionally, the inhomogeneous distribution of the electric field results in a locally increased electric field experienced by the polymer matrix between the conductive NPs, which has a detrimental effect on the overall dielectric breakdown strength.

Recently, an enhanced dielectric breakdown strength was reported in polymer nanocomposites with Ag NPs at a filler loading close to the percolation threshold.[25] The small Ag NPs act as traps for the electrons and locally store the charge in the nanocomposite, facilitated by interfacial polarization. A similar increase in $\varepsilon_r$ was observed in multiwalled carbon nanotubes in PVDF, attributed to the strong molecular level interactions at the interface of the conductive filler and the polymer matrix.[20]

Scanning probe techniques allow for the investigation of interfaces at the nanoscale.[16,26,27] The charge state in grafted organic monolayers on a silicon substrate, with Au NPs deposited on top has been studied using such techniques.[28,29] Stable charge retention in the Au NPs, attributed to polaron effects at the amine functional group, was observed when the organic monolayer was terminated by $-CONH(CH_2)_2NH_2$. This charge retention at the organic-inorganic interface is expected to affect the dielectric breakdown behavior of these molecular junctions. We therefore performed an in-depth study of the dielectric breakdown behavior of a similar set of molecular junctions and studied the nanoscale mechanism of charge transfer at the organic-inorganic interface. In addition, we extended these studies to the meso- and macroscale by investigating the dielectric breakdown and charge retention in thin and thick films.

Here, we report the influence of the organic-inorganic interface on charge retention and dielectric breakdown behavior in nanodielectric materials, from macroscopic samples down to a single nanoscale interface. The three different length scales studied are: 1) end-functionalized self-assembled monolayers (SAMs, ~2 nm) in contact with Au NPs; 2) polystyrene (PS)/Au NP thin films (~100 nm); and 3) PS/Au NP thick films (~2-3 μm). The nanoscale properties of the SAMs and thin films were measured using KPFM and Conductive Atomic Force Microscopy (C-AFM). The bulk properties of the thick films were measured using a specialized high-voltage set-up.

## RESULTS AND DISCUSSION

### Synthesis and Characterization of SAMs Decorated with Au NPs

Self-assembled monolayers (SAMs) decorated with Au NPs are used as a model system in order to study the charge transfer at the interface between different terminated SAMs and Au NPs (Figure 1A). The SAMs are grown on ultraflat (approaching atomic flatness) template stripped gold ($Au^{TS}$) surfaces, and Au NPs with a diameter of 12.5 ± 1.6 nm (Figure S1) are deposited on the SAM surface.

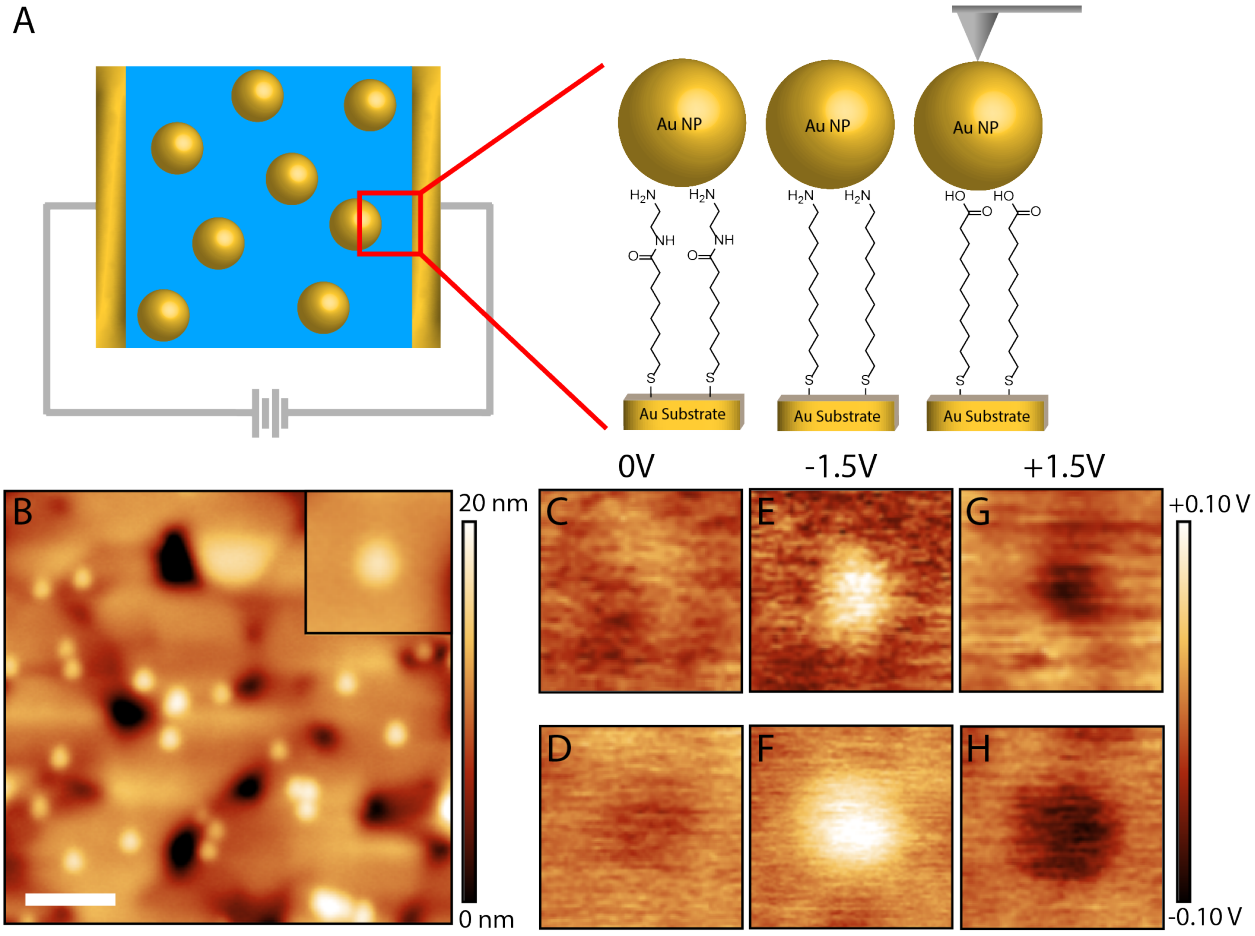


**Figure 1.** A) Schematic of the molecular junction mimicking the interface in a nanocomposite used as dielectric in a parallel plate capacitor. B) AFM image of the topography of the -$(CH_2)_4NH_2$ terminated SAM with deposited Au NPs. The scalebar is 200 nm. Inset: zoom on a single supported NP. C-H) KPFM images showing the CPD of a single Au NP after applying a bias of 0V (C-D), -1.5V (E-F), and +1.5V (G-H), on the -$CONH(CH_2)_2NH_2$ (C, E, and G), and on the -$(CH_2)_4NH_2$ terminated SAM (D, F, and H).

The molecular junction mimics the organic-inorganic interface, here between the SAM and the Au NP, which is typically present in dielectric nanocomposites (Figure 1A). Different end-functionalized alkanethiols were used to form the SAMs, with the formula -$S(CH_2)_7$-T where T =

$CONH(CH_2)_2NH_2$, $(CH_2)_4NH_2$, or $(CH_2)_3COOH$ (Figure 1A, right). The molecules were synthesized following previously reported procedures and characterized by $^1$H-NMR, $^{13}$C-NMR, and ESI-HRMS (see Supplementary Information for full experimental procedures and characterization).[29,30] The final structure of $-S(CH_2)_7-CONH(CH_2)_2NH_2$ was characterized by the surface sensitive techniques X-ray photoelectron spectroscopy (XPS) (Figure S2) and grazing angle attenuated total reflectance Fourier-transform infrared spectroscopy (GATR-FTIR) (Figure S3), which confirmed the presence of the desired functional groups. The sample morphology and Au NP deposition were imaged by AFM (Figure 1B). The comparable chain length of the three SAMs will later allow a quantitative comparison of the observed behavior solely due to the nature of the end tail in contact with the Au NP, with no effect of differences in the thickness of the SAM.

**Chemically Specific Charge Retention at the SAM/Au NP Interface**

Nanoscale charge manipulation and surface potential measurements were used to probe the charge retention capabilities of our three model SAM/Au NP interfaces. To achieve this, we performed KPFM measurements, a non-contact scanning probe microscopy technique that allowed us to simultaneously measure the topography and the contact potential difference (CPD) of the system and monitor the charge state of the scanned area (Figure 1C-H). An initial image of the surface potential ensures the uniformity of the charge over the SAM regions and NPs on top of the SAM (Figure 1C-D). Next, we use the AFM tip to directly contact the gold NP and inject charges locally into the junction. A second KPFM measurement is carried out afterwards in order to map the resulting trapped charges with nanoscale resolution following an existing procedure.[28]

From these charge-injection measurement results, we observe noticeable charge retention capabilities of the two molecules with an amine-terminating group. Both the application of a negative (-1.5V) or positive (+1.5V) potential while contacting the NP result respectively in an increase (Figure 1E-F) and decrease (Figure 1G-H) of the measured CPD. Thus, electrons as well as holes are similarly trapped at the interface. On the other hand, the Au NPs on the -$(CH_2)_3COOH$ terminated SAM did not exhibit any charge retention under the same charge injection protocol (Figure S4). These observations are in line with our previous findings where a grafted monolayer on a Si surface terminated by -$CONH(CH_2)_2NH_2$ interfacing with the Au NPs exhibited charge retention, whilst the -$(CH_2)_3COOH$ terminated grafted monolayer interfacing with Au NPs did not.[28] Here we observe that solely the presence of an amine group at the interface with the Au NP is sufficient to allow for charge retention, thus questioning the mechanism previously proposed.

The observation of this chemically specific charge retention can be explained by considering the Maxwell-Wagner-Sillar (MWS) interfacial polarization.[31–34] According to this model, a capacitive current flowing across an interface between two dielectric materials with different relaxation time $\tau = \varepsilon_r/\sigma$, where $\sigma$ is the conductivity of the material, provokes the accumulation of charges at this interface. The MWS polarization is further enhanced when there is a significant interaction between the two components at the interface.[20] An amine functional group binds stronger to Au than a carboxy functional group,[35] and thus the interfacial polarization is enhanced following the MWS model. A significant energy barrier for charge transport across the Au NP-SAM interfacial area suppresses leakage current, and the charge carriers are retained at the interface.[36]

**Density Functional Theory Calculations**

Density functional theory (DFT) calculations were performed to understand the observed charge retention in the presence of specific organic-inorganic interfaces in the SAM/Au NP system. The electronic properties and geometry of molecules terminated by -$NH_2$ and -COOH in contact with a (111) Au surface were simulated to investigate the existence of charge-induced states that could retain charge at the interface. We chose a simplified system consisting of an Au nanocube with one face covered with an organic monolayer terminated by - $NH_2$ and -COOH, as shown in Figure 2.

The experimental charge injection was mimicked computationally by controlling the total charge state of the system. For both the -$NH_2$ and -COOH terminated molecules two stable geometries were found after structural relaxation for two different charge states, one neutral, and the other with a positive charge state created by removing 4 electrons. (Figure 2A-D).

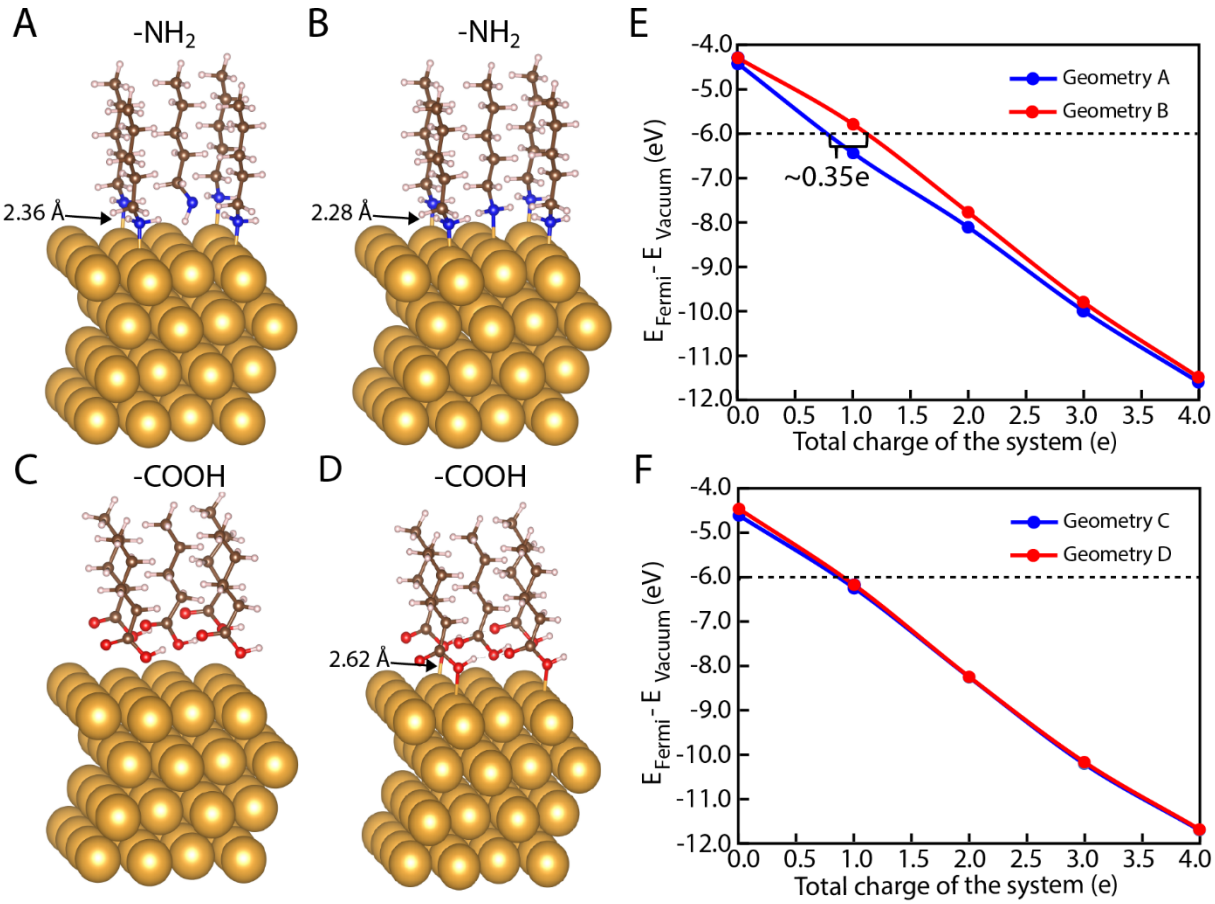


**Figure 2.** Optimized geometries of A), C) neutral and B), D) +4e charged systems of the A-B) -$NH_2$ and C-D) -COOH interfacing with the Au surface. Fermi energy with respect to the vacuum level of neutral and +4e optimized geometries at different charge states for E) -$NH_2$ and F) -COOH interfacing with the Au surface.

In the case of the -$NH_2$/Au interface, in the neutral state most but not all molecules are bound to the Au surface by the amine group through dative bonding between Au and N. Under the simulated electric field of the charged system, all molecules are bound and the bond length between the molecules and the Au surface decreased, indicating an increased bond strength in this geometry. On the other hand, the -COOH/Au system shows no binding of the carboxylic

acid group to the Au surface in the neutral state and with only a few, loosely bound molecules in the charged state resulting in geometry D.

Charging is manifested by the change of the Fermi and vacuum energy levels, as shown in Figure S5 and plotted in Figure 2E and F as the difference between these energies for a few charge states (number of electrons extracted). A remarkable charge difference ($\Delta Q$) is observed for the -$NH_2$/Au system for a given Fermi energy (*e.g.* at $E_{Fermi}$ = 6.0 eV, $\Delta Q$ = 0.35e) between geometry A and B, as shown in Figure 2E. This illustrates the ability of the -$NH_2$/Au interface to have a charge-induced geometrical change that is capable of retaining a significant amount of charge. On the other hand, for the -COOH/Au system in Figure 2F, $\Delta Q$ is almost negligible at the same Fermi energy.

The charge transfer that takes place in the system can be visualized by analyzing the charge density differences, showing the electron transfer between the molecules and the Au surface (Figure S6). For the -$NH_2$/Au system, we observe a large shift in charge density at the interface, where electrons are pulled away from the H and C atoms towards the N atom as well as the Au surface. We observe this charge transfer for geometry A as well as B, with the charge transfer being more pronounced for geometry B. This illustrates the highly polarizable nature of the -$NH_2$/Au interface. On the other hand, for the -COOH/Au system, no charge transfer is observed in geometry C. Even in the case of geometry D, only a negligible charge transfer is observed, indicating no significant interactions at this interface and no possibility of charge accumulation and thus charge retention at this interface. These results are in accordance with the experimental KPFM results indicating a chemically specific charge retention where the interface plays a crucial role.

**Dielectric Breakdown of SAMs**

The dielectric breakdown properties of the above-mentioned SAMs decorated with Au NPs were investigated. The electrical properties of SAMs of alkanethiolates on gold have been extensively investigated and the breakdown voltage ($V_{br}$) is known to be improved by increasing the monolayer thickness, or its ordering and packing density on the substrate.[37–40] In our system, these parameters are constant between the different samples. We were therefore able to extract purely the influence of the SAM/Au NP interface and relate this to its charge retention capabilities.

The dielectric breakdown behavior of the different functionalized SAMs was investigated using C-AFM. A linearly increasing voltage (~0.2 V/s) was applied between the AFM tip and the underlying gold substrate while gently contacting the sample. The measurements were performed both on the bare SAM and on the Au NPs deposited on top of the SAM (Figure 3A, inset). The appearance of a significant current (>5nA) flowing through the junction (Figure 3A) indicates a breakdown event and thus allows the determination of $V_{br}$.

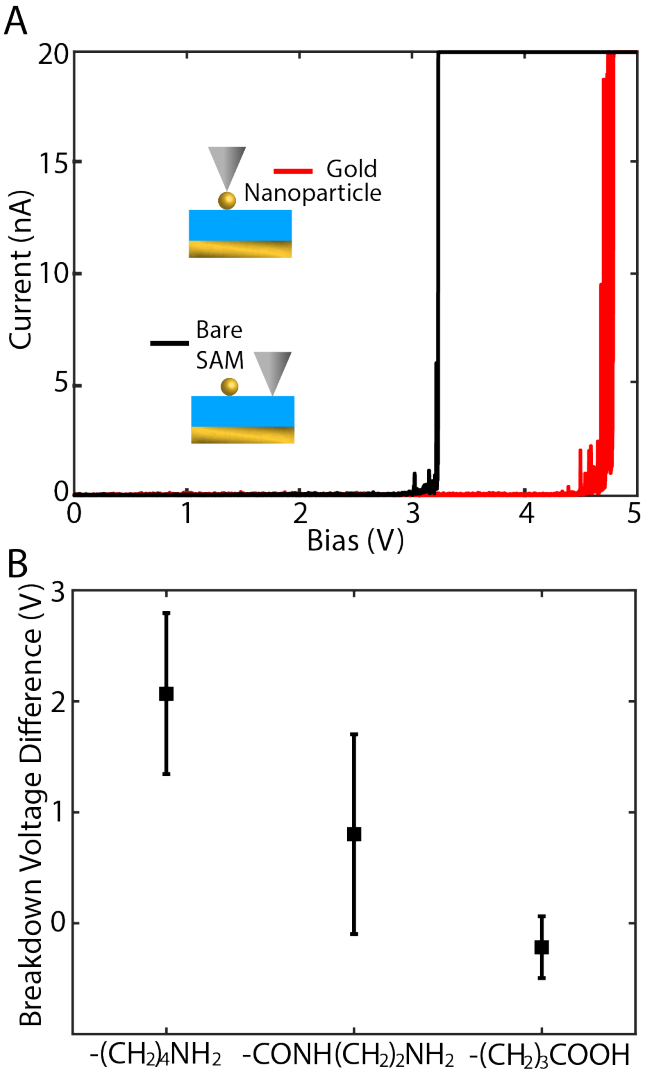


**Figure 3.** Breakdown measurements on the molecular junctions by C-AFM. A) I-V traces of the -$(CH_2)_4NH_2$ terminated SAM, illustrating the difference in breakdown voltage between the bare SAM and the SAM that has an interface with the Au NP. B) The breakdown voltage difference between contacting the bare SAM and contacting the Au NP deposited on top of the SAM.

When directly contacting the SAM, similar breakdown strengths are observed for the different SAMs used in this study (Figure S7). Considering a molecule length of around ~1.6 nm (which translates to a SAM thickness of ~1.4 nm taking into account the 30° tilt angle of SAMs on a

gold substrate, more details in Figure S7),[41] this corresponds to an $E_{br}$ of about 1.5 GV/m which is comparable to values previously observed in the literature.[39] For the -$(CH_2)_4NH_2$ terminated SAM, a remarkable breakdown voltage difference of ~2V is observed between contacting the bare SAM (Figure 3A, black curve) or an Au NP on top of the SAM (Figure 3A, red curve). The difference between the two cases is the presence of the SAM-Au NP interface instead of the SAM-PtIr AFM tip. The same measurements were performed on the -$CONH(CH_2)_2NH_2$ terminated SAM and the -$(CH_2)_3COOH$ terminated SAM. In the case of the -$CONH(CH_2)_2NH_2$ terminated SAM, a slightly smaller yet similar effect was observed. This illustrates the fact that the amine/Au NP interface has a significant and positive influence on the dielectric breakdown strength of the material. The breakdown voltage difference is zero, within experimental error, for the -$(CH_2)_3COOH$ terminated SAM (Figure 3B and Figure S7A). This observation highlights the impact of the presence of the different organic-inorganic interfaces on the breakdown response of the material. Interestingly, such observations seem to draw a direct link between the charge retention capabilities of the organic/inorganic interface and its breakdown capabilities. A localized interfacial polarization created at the amine terminated SAM-Au NP interface would prevent charge carrier propagation across the interface as they get trapped, implying a synergistic effect between charge retention and enhanced breakdown capabilities in these systems.

**Impact of the Inorganic NPs in Thin Polymer Films**

From these model system experiments on a single interface, we move on to study the effect of the incorporation of the Au NP inorganic fillers into a low-cost commodity polymer matrix. Firstly, thin films in the range of 50-200 nm were prepared to be able to use scanning probe microscopy techniques to study their properties. Neat polystyrene containing 0.016 v% of Au

NPs were prepared by spin coating from toluene. The Au NPs are covered in oleylamine ligands (Figure S8A-B), thus exhibiting the amine/Au NP interface that showed promising charge retention and breakdown strength enhancement on the single interface length scale. TEM imaging of the films (Figure 4A and Figure S8C) evidence the uniform distribution of the Au NPs, overall uniform structure of the film, and provide an estimate of the mean in-plane NPs distance ~50nm (Figure S8D), which is below the percolation threshold.[42]

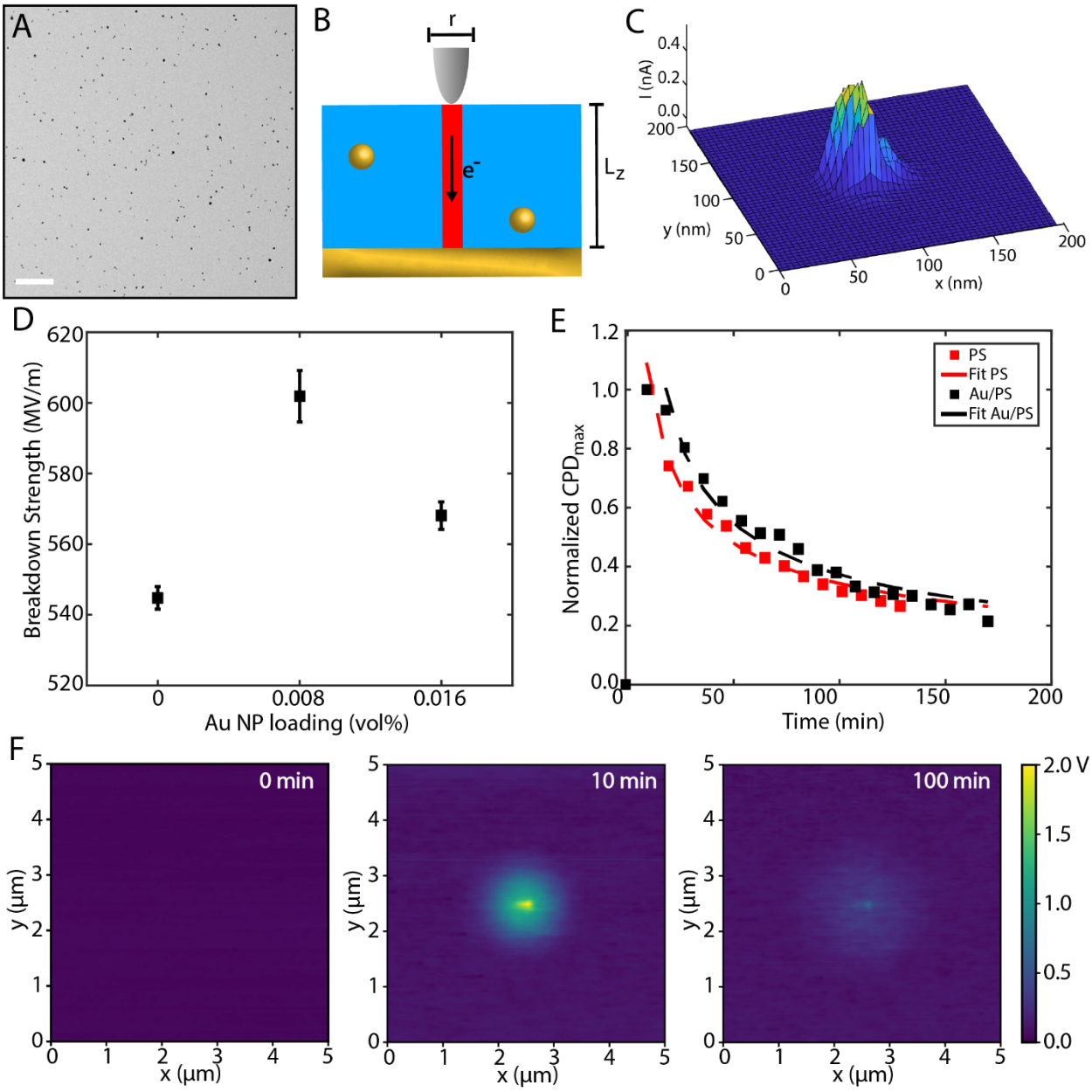


**Figure 4.** A) A top-down view TEM image of a 78 nm thin film of 0.016v% in polystyrene. Scalebar is 200 nm. B) Schematic of the ballistic electronic conduction in the film after breakdown. C) Conductive map of the thin film after dielectric breakdown. D) Dielectric breakdown strength of the thin films measured by C-AFM for different Au NP loadings. E) Decay of the maximum of the CPD over time for neat PS (red) and the 0.016 v% PS/Au NP nanocomposite (black). The dashed lines show the corresponding power-law fittings. F) Map of

the CPD, from left to right before applying a bias, 10 min, and 100 min after applying 32V at the center of the sample.

Similar to the SAM measurements, C-AFM allows us to probe the breakdown voltage and electronic properties of the thin films (Figure 4B-D). By increasing the potential applied across the thin film, a current is eventually measured, indicating the breakdown of the film. We observe a slight increase of the breakdown electric field from ~540 MV/m for the neat PS film up to ~600 MV/m with the presence of Au NPs for ~200 nm thick films (Figure 4D). Interestingly, for ~60 nm thick films, we do not observe any difference in the mean value, and report some dramatically small breakdown values for certain locations on the film containing Au NPs compared to neat PS films (Figure S9). For this thickness, the presence of the NPs would lead to significant local structural defects over a length scale comparable with the entire film size, which jeopardizes the breakdown strength of the film. These observations are in accordance with a ballistic electronic conduction in the film after breakdown (Figure 4B) as expected for such thin film with a very small probe size (~10 nm).

In the case of these thin films, as breakdown occurs, electrons start to flow across the entire polymer film. This electron flow under high electric field strongly damages the film. In order to probe the changes in the electronic properties of the film caused by the breakdown event, we perform local conductive mapping around the position where breakdown was induced (Figure 4C). While imposing a constant voltage of approximately half the measured breakdown voltage, to not induce any additional breakdown event, we observe a conductive pathway spanning a few tens of nanometers laterally around the initial breakdown measurement position. This illustrates the irreversible change in the chemical nature of the nanocomposite after breakdown.

Using KPFM, we then monitor the spatial distribution and diffusion of charges injected locally with the AFM tip. A contact potential difference (CPD) map obtained after imposing a bias potential below $V_{br}$ (32 V for 1s) shows the presence of trapped charge, manifested by the contact potential difference measured by the AFM tip, with a magnitude of ~2 V over several micrometers (Figure 4E-F). Within a few hours, the trapped charges slowly dissipate. As expected for a diffusion controlled process, the evolution of the CPD maximum $CPD_{max}$ over time displays a power-law decrease, $CPD_{max}/CPD_0 \sim t^{-d/2}$ with time, t, where $CPD_0$ is the CPD value at t=0 and d is the dimension of the diffusion process. From fitting the measured CPD decay, which happens due to diffusion of the charge, we obtain an exponent of ~ 0.5 (Figure 4E). This corresponds to a 1D diffusion process in which charges that initially spread laterally along the surface would diffuse directly towards the back electrode.[43] Similar charge decay times, within the experimental resolution, are observed for neat PS films (Figure 4E, red) and PS/Au NP nanocomposites (Figure 4E, black). The nanocomposite exhibits an initial delay ~ 10 min in the CPD decrease, which may be attributed to enhanced charge retention. Eventually, for both samples, the evolution deviates from the fit at longer times (> 60 minutes). An increased rate of decay was observed after the film broke down (Figure S10). The small conductive pathway in the vicinity of the contact (Figure 4C) is likely to contribute to accelerated charge diffusion, leading to a faster decay of the charge.

Overall, considering the reduced NP loading and the small lateral size of the AFM probe, only a very small number of NPs, if any, will be in the pathway between the AFM tip and the back electrode (Figure 4C). Therefore, this geometry mainly probes the polymer matrix dielectric response with variations only observed for the thickest ~200 nm films. For thinner films, the NPs are not effectively trapping and blocking the charge, as not enough particles are present in the

pathway in the thin film. Larger top electrodes are required to reach a diffusive conduction regime and thicker films are subsequently needed in this case for mechanical stability.

**Thick films with enhanced dielectric properties**

Thicker films (~2-3 μm) of PS with different Au NP loadings were prepared by drop casting from toluene. The same Au NPs as for the thin films were used, which are covered in oleylamine ligands to incorporate the amine/Au NP interface into the nanocomposite. Dielectric breakdown and electric displacement-electric field (*D*-*E*) loop tests were performed on a free-standing film sandwiched between two gold electrodes. The PS/Au NP nanocomposites exhibit remarkably enhanced breakdown strength and energy storage capabilities compared to neat PS.

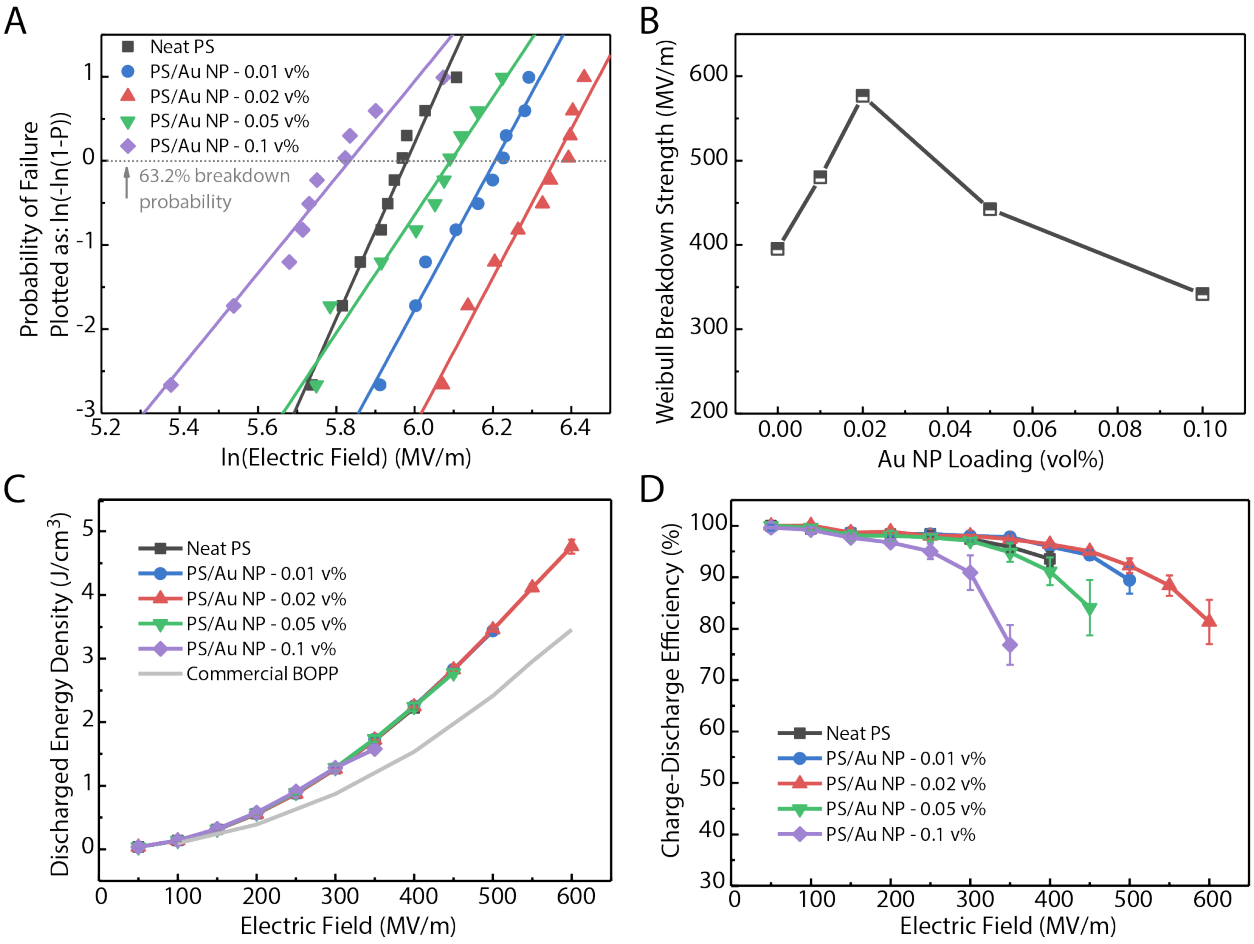


**Figure 5.** Dielectric breakdown properties and capacitive energy storage performance. A) Weibull distribution of the breakdown strength. B) Dependence of the dielectric breakdown strength on the Au NP loading. C) Discharged energy densities for the PS/Au NP nanocomposites, neat PS, and commercial BOPP. BOPP data is derived from literature.[44] D) Charge-discharge efficiencies of neat PS and the PS/Au NP nanocomposites.

Figure 5A shows the Weibull plots associated with the different NP loadings. The fitting model is based on a two-parameter Weibull statistic that can be described as

$$P(E) = 1 - \exp(-(E/\alpha)^{\beta})$$

where $P(E)$ is the cumulative probability of dielectric failure, $E$ is the measured dielectric breakdown field, and $\alpha$ is the scale parameter of the characteristic breakdown strength which corresponds to a failure probability of 63.2%, known as the Weibull breakdown strength. The shape parameter $\beta$ is associated with the scatter of data. A higher $\beta$ value signifies a narrower data spread. At least 10 measurements were performed for each Weibull fitting.

As shown in Figures 5A and B, and Table S1, the Weibull dielectric breakdown strength improved initially with increasing Au NP loading from 395.2 MV/m of neat PS and achieved its peak value of 576.6 MV/m for the nanocomposite with 0.02 v% NP loading. With further increase of the Au NP loading, the breakdown strength decreases, which can likely be attributed to the formation of local conductive channels across interfacial interaction area of adjacent Au NPs.

Additionally, the capacitive energy storage performance was studied, and the corresponding *D*-*E* loops can be found in Figure S11. Benefiting from the substantially enhanced $E_{br}$, the nanocomposite film can withstand higher electric fields. Consequently, a maximum discharged energy density of 4.76 J/cm$^3$ was obtained at 600 MV/m using the 0.02 vol% PS/Au NP nanocomposite, which far exceeds neat PS (2.22 J/cm$^3$) and the state-of-the-art commercial biaxially oriented polypropylene (BOPP) film capacitor (3.46 J/cm$^3$) (Figure 5C).[44] Surprisingly, the charge-discharge efficiency also increased upon the incorporation of Au NPs. For instance, the 0.02 vol% PS/Au NP nanocomposite retains a charge-discharge efficiency of >90% at 500 MV/m (Figure 5D). The higher charge-discharge efficiency suggests a lower leakage current, which could be contributed to the high MWS interfacial polarization at the amine/Au NP interface that generates trap sites to suppress charge transport, which is in line with what was observed at the single interface measurements in the SAM/Au NP system. It also indicates a

highly localized polarization at the organic-inorganic interface, that does not extend into the polymer matrix. The simultaneous increase in breakdown strength and discharged energy density along with improved charge-discharge efficiency in the PS/Au NP nanocomposites suggests that the strong and synergistic interactions between the organic/inorganic materials at the interface play a prominent role in determining the macroscale dielectric properties of these materials.

## CONCLUSIONS

Combining experiments on samples spanning three orders of magnitude in length scale, we obtain a detailed understanding of the mechanisms of charge retention and dielectric strength in nanocomposites. Using Au NPs on SAMs, we uncover the relevance of the chemical nature of the interface on its ability to retain charges. Amine terminated molecules in contact with Au NPs therefore show higher charge retention capabilities and higher breakdown strength compared with carboxylic acid terminated molecules. DFT calculations suggest a geometric change that allows for significant charge retention at the -$NH_2$/Au interface, which is emphasized by the calculated charge density shift at that specific organic-inorganic interface. By using metallic NPs as fillers in tens to hundreds of nanometers thick polymer films, we further highlight the impact of the presence of these organic/inorganic interfaces on the overall material properties. While having a limited impact on the dielectric properties at this mesoscale, the presence of these inorganic fillers provokes a remarkable enhancement in breakdown strength for macroscale (~2-3 um) samples. The results of this work clarify the effect and importance of the interface between the inorganic NP and an organic molecule on the dielectric breakdown behavior. Our findings shed light on the peculiar charge retention mechanism taking place at the organic/inorganic interface, highlighting its chemical selectivity. The eventual impact on the breakdown behavior

of the material turns out to depend largely on the system geometries and NP loading, favoring different electron conduction regimes. Lastly, a deeper understanding of these different phenomena point towards a future advancement of the rational design of nanocomposites with enhanced dielectric capabilities.

METHODS

**Synthesis and Formation of SAMs of Alkanethiolates**

The end-functionalized alkanethiolates were synthesized following previously reported procedures.[29,30] The molecules were characterized by $^{1}$H-NMR, $^{13}$C-NMR, and ESI-HRMS. Full synthetic procedure and characterization data can be found in the Supporting Information. The SAMs were formed on a template-stripped gold substrate (purchased from Platypus Technologies) by submerging the substrate in a 1 mM solution of the desired molecule in ethanol purged with Ar for 20 min. The substrate was incubated under Ar in the dark, overnight. After incubation, the substrate was removed and washed with ~10 mL of ethanol and dried under a gentle stream of $N_2$. The formed SAMs were characterized by XPS and GATR-FTIR.

**Synthesis of Gold Nanoparticles**

*Citrate-capped nanoparticles* (12.5 ± 1.6 nm) used for deposition onto the SAM were synthesized according to the Turkevich Frens method.[45,46] The citrate ligand was chosen to prevent aggregation of the Au NPs, thanks to the electrostatic repulsion from the negatively charged citrate layer. Since the binding of the citrate with Au NPs is extremely weak, it can easily be replaced by other molecules. The Au NPs were characterized by TEM and subsequently deposited from the solution to the sample by dipping the gold substrate with the SAM into the gold colloidal solution for 90 min. Afterwards, the substrate was removed, rinsed with ultrapure water, and dried under a gentle stream of N2.

*Oleylamine-capped gold nanoparticles* (6.2 ± 0.8 nm) for use in the thin and thick films were prepared according to literature.[47] The Au NPs were washed and precipitated by acetone/ methanol and redispersed in toluene with a concentration of 20 mg/mL.

**Thin Film Preparation**

Polystyrene (192,000 molecular weight (SEC)) was dissolved in toluene with a concentration of 35 mg/mL and sonicated until fully dissolved. Afterwards, 5 μL of the oleylamine capped Au NPs (20 mg/mL in toluene) was added to 2 mL of the PS solution and it was mixed thoroughly. Next, 100 μL of the PS/Au NP solution was used for spin coating the solution onto the substrate (~200 nm of Au deposited onto mica by vapor deposition). Different thicknesses of the thin film, and different NP loadings were achieved by altering the concentrations of the solutions. The thickness of the thin films is measured by Filmetrics.

**Thick Film Device Preparation**

Polystyrene (280,000 molecular weight (SEC)) was dissolved in toluene and stirred for 24 h to yield clear solutions. Afterward, the solution was mixed with selected volume percentages of the oleylamine covered Au NPs. The mixture was sealed and sonicated for 30 min and drop-cast onto pre-cleaned glass slides in an air-circulating oven at room temperature for 12 h. The resulting polymer composite films self-peeled off from glass slides in deionized water, followed by a thermal treatment step at 105 $^{o}$C for 24 h in a vacuum oven to remove moisture and residual solvent. Neat PS films were prepared in the same manner. The thickness of the casted free-standing films was controlled to be around 2-3 μm. A gold electrode (4 mm$^2$ area with 20 nm thickness) was deposited on both sides of the polymer film using a thermal evaporator (MBRAUN, Germany) for dielectric characterization.

**Transmission Electron Microscopy**

TEM images were obtained with a FEI Tecnai T20 equipped with a Gatan SC200 CCD camera and LaB6 filament operated at 200 kV. TEM samples were obtained by drop casting 10 μL of a dilute NP solution onto a carbon support with 400 copper mesh and letting the solvent evaporate.

**X-ray Photoelectron Spectroscopy**

XPS measurements were performed on a K-Alpha Plus XPS/UPS using a monochromatic Al X-ray source with a spot size ranging from 30-400 μm. SAMs were used directly after preparation to ensure the least contamination of the surface. The survey was averaged of 10 measurements. On the energy ranges for the atoms of interest: C, N, O, S, and Au, 50 scans were performed.

**Grazing Angle Attenuated Total Reflectance Fourier-Transform Infrared Spectroscopy**

GATR-FTIR measurements were performed on a Nicolet iS50 with a variable angle GATR (Vari-GATR) accessory from Harrick Scientific with a germanium crystal and MCT detector. Measurements were performed at an angle of 62.5° and in the range of 600-4000 $cm^{-1}$.

**Atomic Force Microscopy**

*Topography measurements*. The AFM measurements were performed using an Asylum Research Cypher VES AFM. All measurements were performed in a Nitrogen satured atmosphere.

*Kelvin-Probe Force Microscopy*. PPP-EFM tips (k ~ 3 N/m) were used for KPFM measurements on the SAM and the thin nanocomposite films. KPFM was performed in Amplitude Modulation mode. A 2kHz electrical excitation, superimposed with the mechanical excitation of the cantilever, was imposed with a magnitude ~2-3 V. The deflection of the cantilever at this modulation frequency was further extracted and kept minimal by application of a constant potential $V_{CPD}$ using a feedback loop.

*Conductive-Atomic Force Microscopy*. CONTPt tips from NanoAndMore with typical stiffness k~ 0.2N/m were used. While contacting the sample, the force is kept small (~20 nN) and the applied voltage is slowly increased (0.2 V/s). On the bare polymer film, we directly apply the electric potential across the SAM. Assuming a good, non-resistive, metallic contact between the

apex of the Pt/IR AFM tip and the Au NP, we can similarly consider that the potential drop is directly applied over the SAM when contacting the Au NP. The tip apex, about a couple of tens of nanometers in diameter, has a size similar to the Au NPs diameter.

**High-Voltage Dielectric Characterization**

To avoid creeping discharge, all the devices for high-voltage dielectric characterizations were immersed in a Galden HT-270 PFPE fluorinated fluid. Dielectric breakdown strengths for the thick films were obtained using a high-voltage amplifier (Trek 610D, PolyK Technologies, LLC, USA) according to an electrostatic pull-down method, where a DC voltage ramp of 200 V/s was applied to the film samples until dielectric failure. Electric displacement-electric field (*D*-*E*) loops were obtained under different applied electric fields using a PK-CPE1801 high-voltage test system containing the same Trek 610D high-voltage amplifier. The voltages with a unipolar triangular waveform were applied at a frequency of 10 Hz.

**Computational Details**

All the electronic structure calculations were performed using spin-polarized density functional theory (DFT) as implemented in Vienna Ab-initio Simulation Package (VASP) with projector-augmented-wave (PAW) pseudopotential to account for core-valence interactions.[48–50]

The exchange-correlation term is approximated using the Perdew-Burke-Ernzerhof (PBE) functional within the generalized gradient approximation (GGA).[51] In addition, we also account for the van der Waals (vdW) interaction via Grimme's zero damping given as DFT-D3 method in VASP.[52] Further, dipole correction is invoked in our calculations to eliminate the pseudo interactions between periodic images in the *z*-direction.

To model the interaction between end-functionalized SAMs in contact with Au NPs, we consider a (4$\times$4) Au(111) surface with a thickness of 4 layers where bottom two layers were

frozen to mimic the bulk. The -$(CH_2)_4NH_2$ and -$(CH_2)_3COOH$ terminated SAMs were modeled with 5 carbon long chain to speed up our calculations. A vacuum of 16 Å is considered along the *z*-direction to avoid unwanted interactions due to the periodic images. A kinetic energy cutoff of 500 eV is used to generate a plane wave basis set and the Brillouin zone was sampled using a 2×2×1 gamma-centered k-points mesh.[53] The convergence criteria for the structural relaxation are set as $10^{-5}$ eV and 0.05 eVÅ$^{-1}$ for self-consistent field (SCF) energies and forces on each atom, respectively.

ASSOCIATED CONTENT

**Supporting Information**.

The Supporting Information is available free of charge.

Synthesis and characterization of molecules by $^{1}$H-NMR, $^{13}$C-NMR, and ESI-HRMS, DFT computational details, TEM images and NP size distribution, surface characterization of the SAMs by XPS and GATR-FTIR, KFPM results on the -COOH terminated SAM, electrostatic potentials and charge retention at the interface calculated by DFT, dielectric breakdown measurements of SAMs and thin films. (PDF)

AUTHOR INFORMATION

**Corresponding Author**

* To whom correspondence may be addressed: mbsalmeron@lbl.gov

**Present Addresses**

A. Paul Alivisatos - Department of Chemistry and Pritzker School of Molecular Engineering, University of Chicago, Chicago, Illinois 60637, United States

**Author Contributions**

The manuscript was written through contributions of all authors. All authors have given approval to the final version of the manuscript.

**Funding Sources**

This work was supported by the U.S. Department of Energy, Office of Science, Office of Basic Energy Sciences, Materials Sciences and Engineering Division, under Contract No. DEAC02-05-CH11231 within the Inorganic/Organic Nanocomposites Program (KC3104).

**Notes**

The authors declare no competing financial interest.

ACKNOWLEDGMENT

This work was supported by the U.S. Department of Energy, Office of Science, Office of Basic Energy Sciences, Materials Sciences and Engineering Division, under Contract No. DEAC02-05-CH11231 within the Inorganic/Organic Nanocomposites Program (KC3104). This research used resources of the National Energy Research Scientific Computing Center (NERSC), a U.S. Department of Energy Office of Science User Facility located at Lawrence Berkeley National Laboratory, operated under Contract No. DE-AC02-05CH11231 using NERSC with computational time allocated by the INCITE program. Part of the work was carried out as a user project at Molecular Foundry, supported by the Office of Science, Office of Basic Energy Sciences, of the U.S. Department of Energy under Contract No. DE-AC02-05CH11231.

REFERENCES


(1) Chu, B.; Zhou, X.; Ren, K.; Neese, B.; Lin, M.; Wang, Q.; Bauer, F.; Zhang, Q. M. A Dielectric Polymer with High Electric Energy Density and Fast Discharge Speed. *Science* **2006**, *313*, 334–336.

(2) Simon, P.; Gogotsi, Y. Materials for Electrochemical Capacitors. *Nat. Mater.* **2008**, *7*, 845–854.

(3) Wang, G.; Lu, Z.; Li, Y.; Li, L.; Ji, H.; Feteira, A.; Zhou, D.; Wang, D.; Zhang, S.; Reaney, I. M. Electroceramics for High-Energy Density Capacitors: Current Status and Future Perspectives. *Chem. Rev.* **2021**, *121*, 6124–6172.

(4) Li, H.; Zhou, Y.; Liu, Y.; Li, L.; Liu, Y.; Wang, Q. Dielectric Polymers for High-Temperature Capacitive Energy Storage. *Chem. Soc. Rev.* **2021**, *50*, 6369–6400.

(5) Feng, Q.-K.; Zhong, S.-L.; Pei, J.-Y.; Zhao, Y.; Zhang, D.-L.; Liu, D.-F.; Zhang, Y.-X.; Dang, Z.-M. Recent Progress and Future Prospects on All-Organic Polymer Dielectrics for Energy Storage Capacitors. *Chem. Rev.* **2022**, *121*, 3820-3878.

(6) Huang, J.; Zhou, J.; Liu, M. Interphase in Polymer Nanocomposites. *JACS Au* **2022**. https://doi.org/10.1021/jacsau.1c00430.

(7) Dang, Z. M.; Yuan, J. K.; Yao, S. H.; Liao, R. J. Flexible Nanodielectric Materials with High Permittivity for Power Energy Storage. *Adv. Mater.* **2013**, *25*, 6334–6365.

(8) Lin, X.; Hu, P.; Jia, Z.; Gao, S. Enhanced Electric Displacement Induces Large Energy Density in Polymer Nanocomposites Containing Core–Shell Structured $BaTiO_3$@$TiO_2$

Nanofibers. *J. Mater. Chem. A* **2016**, *4*, 2314–2320.

(9) Roy, M.; Nelson, J. K.; MacCrone, R. K.; Schadler, L. S.; Reed, C. W.; Keefe, R.; Zenger, W. Polymer Nanocomposite Dielectrics - The Role of the Interface. *IEEE Trans. Dielectr. Electr. Insul.* **2005**, *12*, 629–642.

(10) Luo, H.; Zhou, X.; Ellingford, C.; Zhang, Y.; Chen, S.; Zhou, K.; Zhang, D.; Bowen, C. R.; Wan, C. Interface Design for High Energy Density Polymer Nanocomposites. *Chem. Soc. Rev.* **2019**, *48*, 4424–4465.

(11) Li, H.; Yang, T.; Zhou, Y.; Ai, D.; Yao, B.; Liu, Y.; Li, L.; Chen, L. Q.; Wang, Q. Enabling High-Energy-Density High-Efficiency Ferroelectric Polymer Nanocomposites with Rationally Designed Nanofillers. *Adv. Funct. Mater.* **2021**, *31*, 2006739.

(12) Huang, X.; Jiang, P. Core-Shell Structured High- k Polymer Nanocomposites for Energy Storage and Dielectric Applications. *Adv. Mater.* **2015**, *27*, 546–554.

(13) Ren, L.; Li, H.; Xie, Z.; Ai, D.; Zhou, Y.; Liu, Y.; Zhang, S.; Yang, L.; Zhao, X.; Peng, Z.; Liao, R.; Wang, Q. High-Temperature High-Energy-Density Dielectric Polymer Nanocomposites Utilizing Inorganic Core–Shell Nanostructured Nanofillers. *Adv. Energy Mater.* **2021**, *11*, 2101297.

(14) Pan, Z.; Yao, L.; Zhai, J.; Fu, D.; Shen, B.; Wang, H. High-Energy-Density Polymer Nanocomposites Composed of Newly Structured One-Dimensional $BaTiO_3$@$Al_2O_3$ Nanofibers. *ACS Appl. Mater. Interfaces* **2017**, *9*, 4024–4033.

(15) Peng, S.; Luo, Z.; Wang, S.; Liang, J.; Yuan, C.; Yuan, Z.; Hu, J.; He, J.; Li, Q. Mapping

the Space Charge at Nanoscale in Dielectric Polymer Nanocomposites. *ACS Appl. Mater. Interfaces* **2020**, *12*, 53425–53434.

(16) Peng, S.; Yang, X.; Yang, Y.; Wang, S.; Zhou, Y.; Hu, J.; Li, Q.; He, J. Direct Detection of Local Electric Polarization in the Interfacial Region in Ferroelectric Polymer Nanocomposites. *Adv. Mater.* **2019**, *31*, 1807722.

(17) Zhang, G.; Li, Q.; Allahyarov, E.; Li, Y.; Zhu, L. Challenges and Opportunities of Polymer Nanodielectrics for Capacitive Energy Storage. *ACS Appl. Mater. Interfaces* **2021**, *13*, 37939-37960.

(18) Dang, Z. M.; Zheng, M. S.; Zha, J. W. 1D/2D Carbon Nanomaterial-Polymer Dielectric Composites with High Permittivity for Power Energy Storage Applications. *Small* **2016**, *12*, 1688–1701.

(19) Qi, L.; Lee, B. I.; Chen, S.; Samuels, W. D.; Exarhos, G. J. High-Dielectric-Constant Silver-Epoxy Composites as Embedded Dielectrics. *Adv. Mater.* **2005**, *17*, 1777–1781.

(20) Yuan, J. K.; Yao, S. H.; Dang, Z. M.; Sylvestre, A.; Genestoux, M.; Bai, J. Giant Dielectric Permittivity Nanocomposites: Realizing True Potential of Pristine Carbon Nanotubes in Polyvinylidene Fluoride Matrix through an Enhanced Interfacial Interaction. *J. Phys. Chem. C* **2011**, *115*, 5515–5521.

(21) Dang, Z. M.; Lin, Y. H.; Nan, C. W. Novel Ferroelectric Polymer Composites with High Dielectric Constants. *Adv. Mater.* **2003**, *15*, 1625–1629.

(22) Nan, C.-W.; Shen, Y.; Ma, J. Physical Properties of Composites Near Percolation. *Annu.*

*Rev. Mater. Res.* **2010**, *40*, 131–151.

(23) Nan, C. W. Physics of Inhomogeneous Inorganic Materials. *Prog. Mater. Sci.* **1993**, *37*, 1–116.

(24) Dang, Z. M.; Nan, C. W.; Xie, D.; Zhang, Y. H.; Tjong, S. C. Dielectric Behavior and Dependence of Percolation Threshold on the Conductivity of Fillers in Polymer-Semiconductor Composites. *Appl. Phys. Lett.* **2004**, *85*, 97–99.

(25) Huang, X.; Zhang, X.; Ren, G. K.; Jiang, J.; Dan, Z.; Zhang, Q.; Zhang, X.; Nan, C. W.; Shen, Y. Non-Intuitive Concomitant Enhancement of Dielectric Permittivity, Breakdown Strength and Energy Density in Percolative Polymer Nanocomposites by Trace Ag Nanodots. *J. Mater. Chem. A* **2019**, *7*, 15198–15206.

(26) Morsch, S.; Bastidas, P. D.; Rowland, S. M. AFM-IR Insights into the Chemistry of Interfacial Tracking. *J. Mater. Chem. A* **2017**, *5*, 24508–24517.

(27) Liu, Y.; Yang, T.; Zhang, B.; Williams, T.; Lin, Y. T.; Li, L.; Zhou, Y.; Lu, W.; Kim, S. H.; Chen, L. Q.; Bernholc, J.; Wang, Q. Structural Insight in the Interfacial Effect in Ferroelectric Polymer Nanocomposites. *Adv. Mater.* **2020**, *32*, 2005431.

(28) Zhang, Y.; Kang, J.; Pluchery, O.; Caillard, L.; Chabal, Y. J.; Wang, L. W.; Sanz, J. F.; Salmeron, M. Nanoimaging of Organic Charge Retention Effects: Implications for Nonvolatile Memory, Neuromorphic Computing, and High Dielectric Breakdown Devices. *ACS Appl. Nano Mater.* **2019**, *2*, 4711–4716.

(29) Casale, S.; Pluchery, O.; Lamic-Humblot, A.-F.; Chabal, Y. J.; Caillard, L.; Zhang, Y.;

Salmeron, M. Sensing the Charge State of Single Gold Nanoparticles via Work Function Measurements. *Nano Lett*. **2014**, *15*, 51–55.

(30) Baghbanzadeh, M.; Pieters, P. F.; Yuan, L.; Collison, D.; Whitesides, G. M. The Rate of Charge Tunneling in EGaIn Junctions Is Not Sensitive to Halogen Substituents at the Self-Assembled Monolayer//$Ga_2O_3$ Interface. *ACS Nano* **2018**, *12*, 10221–10230.

(31) Nelson, J. K.; Fothergill, J. C. Internal Charge Behaviour of Nanocomposites. *Nanotechnology* **2004**, *15*, 586–595.

(32) Tsangaris, G. M.; Kouloumbi, N.; Kyvelidis, S. Interfacial Relaxation Phenomena in Particulate Composites of Epoxy Resin with Copper or Iron Particles. *Mater. Chem. Phys*. **1996**, *44*, 245–250.

(33) Tamura, R.; Lim, E.; Manaka, T.; Iwamoto, M. Analysis of Pentacene Field Effect Transistor as a Maxwell-Wagner Effect Element. *J. Appl. Phys*. **2006**, *100*, 114515.

(34) Dang, Z. M.; Wang, L.; Yin, Y.; Zhang, Q.; Lei, Q. Q. Giant Dielectric Permittivities in Functionalized Carbon-Nanotube/ Electroactive-Polymer Nanocomposites. *Adv. Mater.* **2007**, *19*, 852–857.

(35) Heuer-Jungemann, A.; Feliu, N.; Bakaimi, I.; Hamaly, M.; Alkilany, A.; Chakraborty, I.; Masood, A.; Casula, M. F.; Kostopoulou, A.; Oh, E.; Susumu, K.; Stewart, M. H.; Medintz, I. L.; Stratakis, E.; Parak, W. J.; Kanaras, A. G. The Role of Ligands in the Chemical Synthesis and Applications of Inorganic Nanoparticles. *Chem. Rev.* **2019**, *119*, 4819–4880.

(36) Li, L.; Cheng, J.; Cheng, Y.; Han, T.; Liang, X.; Zhao, Y.; Zhao, G.; Dong, L. Polymer Dielectrics Exhibiting an Anomalously Improved Dielectric Constant Simultaneously Achieved High Energy Density and Efficiency Enabled by CdSe/$Cd_{1-x}Zn_xS$ Quantum Dots. *J. Mater. Chem. A* **2020**, *8*, 13659–13670.

(37) Haag, R.; Rampi, M. A.; Holmlin, R. E.; Whitesides, G. M. Electrical Breakdown of Aliphatic and Aromatic Self-Assembled Monolayers Used as Nanometer-Thick Organic Dielectrics. *J. Am. Chem. Soc.* **1999**, *121*, 7895–7906.

(38) Zhang, Y.; Qiu, X.; Gordiichuk, P.; Soni, S.; Krijger, T. L.; Herrmann, A.; Chiechi, R. C. Mechanically and Electrically Robust Self-Assembled Monolayers for Large-Area Tunneling Junctions. *J. Phys. Chem. C* **2017**, *121*, 14920-14928.

(39) Yuan, L.; Jiang, L.; Nijhuis, C. A. The Drive Force of Electrical Breakdown of Large-Area Molecular Tunnel Junctions. *Adv. Funct. Mater.* **2018**, *28*, 1801710.

(40) Kong, G. D.; Song, H.; Yoon, S.; Kang, H.; Chang, R.; Yoon, H. J. Interstitially Mixed Self-Assembled Monolayers Enhance Electrical Stability of Molecular Junctions. *Nano Lett.* **2021**, *21*, 3162-3169.

(41) Love, J. C.; Estroff, L. A.; Kriebel, J. K.; Nuzzo, R. G.; Whitesides, G. M. Self-Assembled Monolayers of Thiolates on Metals as a Form of Nanotechnology. *Chem. Rev.* **2005**, *105*, 1103–1170.

(42) Tanaka, T.; Kozako, M.; Fuse, N.; Ohki, Y. Proposal of a Multi-Core Model for Polymer Nanocomposite Dielectrics. *IEEE Trans. Dielectr. Electr. Insul.* **2005**, *12*, 669–681.

(43) Knorr, N.; Rosselli, S.; Nelles, G. Surface-Potential Decay of Biased-Probe Contact-Charged Amorphous Polymer Films. *J. Appl. Phys.* **2010**, *107*, 13–21.

(44) Li, H.; Gadinski, M. R.; Huang, Y.; Ren, L.; Zhou, Y.; Ai, D.; Han, Z.; Yao, B.; Wang, Q. Crosslinked Fluoropolymers Exhibiting Superior High-Temperature Energy Density and Charge-Discharge Efficiency. *Energy Environ. Sci.* **2020**, *13*, 1279–1286.

(45) Turkevich, J.; Stevenson, P. C.; Hillier, J. A Study of the Nucleation and Growth Processes in the Synthesis of Colloidal Gold. *Discuss. Faraday Soc.* **1951**, *11*, 55-75.

(46) Frens, G. Controlled Nucleation for the Regulation of the Particle Size in Monodisperse Gold Suspensions. *Nat. Phys. Sci.* **1973**, *241*, 20–22.

(47) Peng, S.; Lee, Y.; Wang, C.; Yin, H.; Dai, S.; Sun, S. A Facile Synthesis of Monodisperse Au Nanoparticles and Their Catalysis of CO Oxidation. *Nano Res.* **2008**, *1*, 229–234.

(48) Kresse, G.; Furthmüller, J. Efficiency of Ab-Initio Total Energy Calculations for Metals and Semiconductors Using a Plane-Wave Basis Set. *Comput. Mater. Sci.* **1996**, *6*, 15–50.

(49) Kresse, G.; Joubert, D. From Ultrasoft Pseudopotentials to the Projector Augmented-Wave Method. *Phys. Rev. B* **1999**, *59*, 1758–1775.

(50) Bloechl, P. E. Projector Augmented-Wave Method. *Phys. Rev. B* **1994**, *50*, 17953–17979.

(51) Perdew, J. P.; Ernzerhof, M.; Burke, K. Rationale for Mixing Exact Exchange with Density Functional Approximations. *J. Chem. Phys.* **1996**, *105*, 9982–9985.

(52) Grimme, S.; Antony, J.; Ehrlich, S.; Krieg, H. A Consistent and Accurate Ab Initio

Parametrization of Density Functional Dispersion Correction (DFT-D) for the 94 Elements H-Pu. *J. Chem. Phys.* **2010**, *132*, 154104.

(53) Monkhorst, H. J.; Pack, J. D. Special Points for Brillouin-Zone Integrations. *Phys. Rev. B* **1976**, *13*, 5188–5192.

TOC GRAPHIC

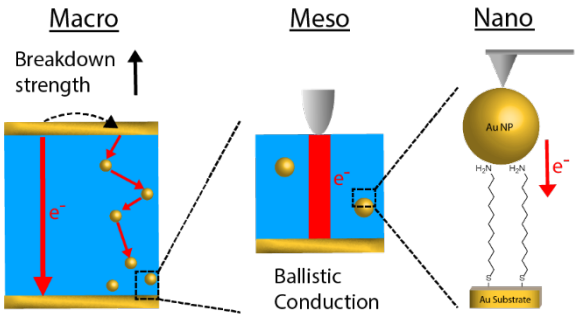
Macro
Meso
Nano
Breakdown strength
e-
e-
Ballistic Conduction
Au NP
e-
Au Substrate